Journal of Materials Chemistry C

PAPER

Check for updates

Application of composition controlled nickel-alloyed iron sulfide pyrite nanocrystal thin films as the hole transport layer in cadmium telluride solar cells†

Ebin Bastola, [ID] Khagendra P. Bhandari and Randy J. Ellingson*

Here, we report hot-injection colloidal synthesis, characterization, and control of electronic conductivity of nickel-alloyed iron sulfide ($Ni_xFe_{1-x}S_2$) pyrite nanocrystals (NCs). The Ni-alloyed iron pyrite NCs were synthesized using iron (Fe) and nickel (Ni) bromides as Fe and Ni sources, and elemental sulfur (S) as a sulfur source. As Ni is incorporated into the iron pyrite (FeS_2) NCs, the X-ray diffraction (XRD) peaks shift towards lower diffraction angles indicating higher lattice constants of the alloyed NCs in accord with Vegard's law. Scherrer-analysis and scanning electron microscopy (SEM) imaging indicate that the average particle sizes of alloyed NCs are smaller compared to pure FeS_2 NCs. In UV-Vis-NIR spectra, the alloyed NCs have higher absorbance in the infrared (IR) region than pure FeS_2 NCs indicating Ni-alloyed NCs have higher densities of mid-band gap defect states. Based on thermal probe and Hall-effect measurements, the majority charge carriers in these alloyed NCs depend upon the material composition. Pure iron pyrite (FeS_2) and $Ni_{0.1}Fe_{0.9}S_2$ NCs show p-type conductivity while $Ni_{0.2}Fe_{0.8}S_2$ and higher Ni concentration alloys exhibit n-type conductivity. Application of these alloyed NC thin films as the hole transport layer for CdTe solar cells revealed that $Ni_{0.05}Fe_{0.95}S_2$ NCs perform best with the average increase in efficiency of $\sim$5%, with the best cell performing up to 8% better than the laboratory standard copper/gold (Cu/Au) cell.

Introduction

Iron disulfide (iron pyrite, FeS_2) is an earth abundant material with lower toxicity than semiconducting materials containing lead or cadmium. Iron pyrite has been investigated over decades as a potential light absorber for photovoltaic application, with only limited success due to a propensity for highly ionized defect states.[1,2] Iron pyrite is a semiconducting material with an indirect band gap of 0.95 eV and absorption coefficient $\geq 10^5$ cm^{-1} in the visible region of light spectrum.[3,4] In recent years, iron pyrite (FeS_2) nanocrystals (NCs) have been investigated to develop low-cost synthetic avenues, and for solution-processed application as counter electrodes in dye-sensitized solar cells,[5] quantum-dot-sensitized solar cells,[6] and in thermoelectric applications.[7,8]

The optical and electronic properties of the FeS_2 can be tailored for specific opto-electronic applications through alloying with other elements.[9–14] Based on a theoretical study, Hu et al. have shown the band gap of iron pyrite can be increased from $\sim$1 eV to 1.2–1.3 eV by replacing 10% of sulfur with oxygen (O)

atoms.[9] However, to the authors' knowledge, no experimental evidence has been reported on incorporating oxygen into FeS_2. The combined effect of Zn alloying and biaxial strain on atomic structure of FeS_2 was previously studied by Xiao et al. using first-principle calculation and found that the band gap of $Fe_{1-x}Zn_xS_2$ alloy increases from 0.95 eV to $\sim$1.14 eV.[12] Buker et al. experimentally showed the incorporation of $\sim$5% Zn in FeS_2 using chemical vapor transport method to increase the band gap of FeS_2.[13] Researchers are still trying to improve the opto-electronic characteristics of FeS_2 by alloying with other transition elements. Nickel disulfide (NiS_2), which exhibits cubic pyrite crystal structure, has been studied as a promising material for photocatalytic water splitting applications to produce hydrogen for electrochemical fuel cells which can in turn be used for vehicle propulsion.[15–17] Nickel iron disulfide ($Ni_xFe_{1-x}S_2$) thin films prepared by electron-beam evaporation have also shown interesting catalytic properties in hydrogen evolution reactions.[18,19]

Several techniques have previously been reported to fabricate both pure and transition-metal-alloyed FeS_2 thin films including molecular beam epitaxy (MBE),[20] chemical vapor transport (CVT) method,[21–24] chemical bath deposition,[25] and electron-beam evaporation.[18] Similarly, reports also exist for the preparation of Ni-alloyed iron sulfide ($Ni_xFe_{1-x}S_2$) thin films using CVT, and chemical bath deposition method.[24,26] Ferrer et al. reported the

Wright Center for Photovoltaics Innovation and Commercialization (PVIC), Department of Physics and Astronomy, University of Toledo, Toledo, Ohio 43606, USA. E-mail: Randy.Ellingson@utoledo.edu
† Electronic supplementary information (ESI) available. See DOI: 10.1039/c7tc00948h

preparation and structural properties of thin films of $Fe_{1-x}Ni_xS_2$ by subsequent sulfuration flash evaporated Fe–Ni layers.[26,27] Similarly, optical and semiconducting properties of NiS_2 thin films deposited on indium tin oxide coated glass substrates were also studied.[28] Since the MBE, CVT and electron-beam evaporation methods require ultra high vacuum or high temperature (or both), and hence the solution-processed synthesis can be an alternative to these methods. The common solution-based methods for the preparation of iron/nickel dichalcogenide NCs are hydrothermal,[29] and solvothermal.[30,31] Preparation of phase-pure materials by hydrothermal or solvothermal techniques requires relatively long reaction time or higher pressure compared to a hot-injection colloidal route; in addition, hot-injection allows one to control NC size and via solvent and surfactant selection, injection temperature, and growth time. In recent years, hot-injection colloidal synthesis has been used to prepare phase-pure iron dichalcogenide NCs such as FeS_2, $FeSe_2$, and $FeTe_2$.[32–34] After synthesis of these colloidal NCs, techniques such as drop-casting, spin coating, and dip-coating can be employed to prepare NC-based thin films at laboratory scale; screen-printing and inkjet printing exist for large scale fabrication. Previously, solution-processed iron pyrite (FeS_2) NC thin films have been successfully applied as hole transport layers (HTLs) in CdS/CdTe and perovskite solar cells.[35,36] Also, inorganic NiO nanoparticles have been used as HTMs in efficient perovskite solar cells.[37] Similarly, solution-based $FeSe_2$ films show very promising results as counter electrodes in sensitized solar cells.[5,38] Though researchers have synthesized phase pure colloidal FeS_2 NCs by hot-injection, there does not exist any report for $Ni_xFe_{1-x}S_2$ alloyed NCs prepared by a hot-injection route. Previously, the synthesis and characterization of Co-alloyed iron pyrite NCs have been reported using hot-injection colloidal method.[14] On alloying Co with iron pyrite NCs, the characteristics such as conductivity, mobility, and carrier concentration increase as the Co fraction increases in the composite NCs. In addition to this, the majority charge carrier type flips from p-type to n-type for Co/Fe ratio above about 25% in Co-alloyed FeS_2 NCs.[14]

Here, we report hot-injection colloidal synthesis, characterization, and the control of electronic conductivity of Ni-doped iron pyrite (FeS_2) NCs. The pure iron pyrite NCs exhibit p-type semiconducting properties with holes as the majority charge carriers, and after doping these NC materials with 20% or higher amount of Ni, the majority charge carriers change to electrons showing n-type conductivity. Hence, the conductivity of the Ni-alloyed iron pyrite NCs depends on the composition of the material. The synthesized Ni-alloyed iron sulfide ($Ni_xFe_{1-x}S_2$) NCs exhibit cubic crystal structure in pyrite phase. We study additional optical, electronic and morphological properties by using UV-Vis-NIR spectroscopy, Hall characterization, scanning electron microscopy (SEM) imaging, and thermal probe to determine the sign of the Seebeck coefficient. The performance of the $Ni_xFe_{1-x}S_2$ thin films as the HTL for CdTe solar cells depends critically on the HTL composition: whereas a $Ni_{0.05}Fe_{0.95}S_2$ HTL slightly increases device efficiency as compared with our standard back contact, a $Ni_{0.2}Fe_{0.8}S_2$ HTL decreased efficiency by ~56%.

Experimental

Chemicals

Nickel(II) bromide ($NiBr_2$, 98%), oleylamine (OLA, 70%), sulfur (S, 99.9%), methanol (CH_3OH, 99.5%) and trioctylphosphine oxide (TOPO) were obtained from Sigma-Aldrich. Iron(II) bromide ($FeBr_2$, anhydrous 99.9%) and chloroform ($CHCl_3$) were purchased from Alfa-Aesar and Fisher-Scientific respectively. All the chemicals were utilized as obtained without further purification.

Nanocrystal synthesis and film preparation

Synthesis of Ni-alloyed iron pyrite nanocrystals employed a method similar to that reported previously for the synthesis of Co-alloyed iron pyrite NCs.[14] For a typical synthesis, 1 mmol iron(II) bromide and nickel(II) bromide in different proportions were taken in a three-neck flask along with 6 mmol TOPO and 20 mL OLA. The three-neck flask was alternately placed under vacuum for one minute and purged with nitrogen gas, repeated 3 times in a standard Schlenk line system. Then, it was heated at a temperature of 170 °C for about 3 hours in a nitrogen environment with continuous stirring. The S precursor was prepared by dissolving 6 mmol of elemental S in 10 mL OLA with ultra-sonication of around 15 minutes. After refluxing the three-neck flask for 3 hours, the S precursor was injected rapidly, the temperature was immediately increased to 220 °C, and the NCs were grown for 2 hours at the same temperature. Then, the heating mantle was removed, and allowed to cool down to room temperature. The product NCs were cleaned using chloroform as solvent and methanol as antisolvent, respectively, three times. The cleaned NCs were dried and stored under nitrogen for further characterization. The characterization of NCs, thin film preparation, and the device fabrication are provided in the ESI.†

Results and discussion

Fig. 1 shows the XRD patterns for $Ni_xFe_{1-x}S_2$ NCs synthesized with different concentrations of Ni starting from $x = 0$ to $x = 1$. The fraction of Ni (x) in the synthesized composite material was calculated by taking the ratio of atomic percentage of Ni to total atomic percentage of Fe and Ni based on the EDS results of the synthesized NCs. The EDS spectrum of pure and Ni-alloyed iron pyrite NCs are shown in Fig. S1 in ESI.† For $x = 0$, the product is pure iron pyrite NCs whose XRD pattern matches exactly with the standard peaks of the pyrite FeS_2 data obtained from MDI JADE software (PDF# 97-063-3254). The XRD peaks of iron pyrite NCs are precisely similar to the previous reports,[32,33] and these NCs have cubic crystal structure with a lattice constant of 5.430 Å belonging to the space group $Pa\bar{3}(205)$. With 0.1 mmol $NiBr_2$ (0.02186 g) and 0.9 mmol $FeBr_2$ (0.1941 g), alloyed NCs were produced with the composition $Ni_{0.1}Fe_{0.9}S_2$ as confirmed by energy dispersive X-ray spectroscopy (EDS) measurement, and the typical XRD pattern shows a shift of 2θ peak positions to lower angles as shown in Fig. 1. The slight decrease in diffraction angle values in the pattern indicates the increase in the lattice constants of the crystal due to the
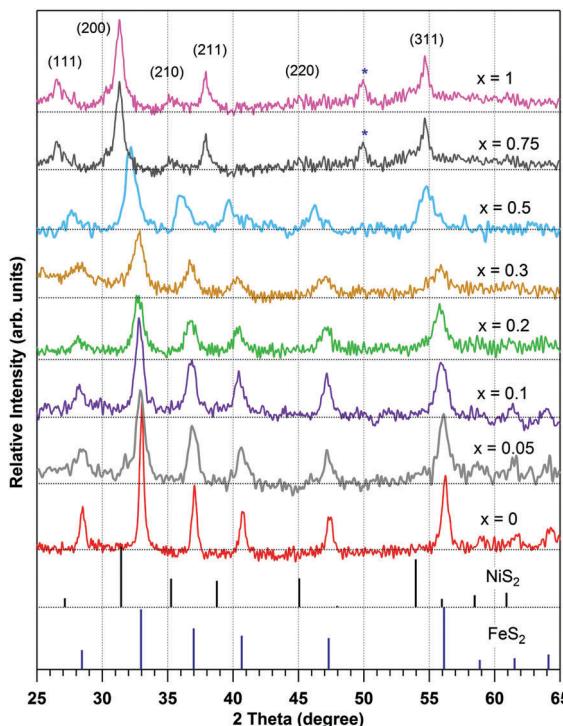
Fig. 1 X-ray diffraction (XRD) pattern of Ni-alloyed iron sulfide ($Ni_xFe_{1-x}S_2$) pyrite nanocrystals with $x = 0$ to 1. The reference lines are for standard iron pyrite (FeS_2) (PDF #97-063-3254), and vaesite (NiS_2) (PDF #98-001-3472) obtained from MDI JADE software. The sharp peaks of these Ni-alloyed iron pyrite NCs confirm the material synthesized is highly crystalline. The peaks marked with * are tentatively assigned to Ni_3S_4 which has face-centered cubic (FCC) crystal structure (see text for discussion).

substitution of Ni atoms ($3d^84s^2$) for Fe atoms ($3d^64s^2$). With the exception of a peak near $2\theta = 50°$ for the $x = 0.75$ and $x = 1.0$ samples, tentatively assigned to Ni_3S_4, no other peaks except pyrite were observed in the XRD pattern indicating highly phase-pure pyrite material. Previously, Ho *et al.* has observed the similar shift in the XRD pattern for $Ni_{0.1}Fe_{0.9}S_2$ single crystals prepared by CVT method.[21] In the similar way, other NCs with different material compositions such as Ni 20%, 30%, 50%, 75%, and 100% were synthesized taking different precursors ratios of Ni and Fe. The EDS analysis of composition of these Ni-alloyed pyrite NCs closely agree with the initial ratio of the $NiBr_2$ to the total amount of $FeBr_2$ and $NiBr_2$ reactants taken during the synthesis. Similarly, with higher concentration of Ni, the peaks shift continuously further towards smaller 2θ values as shown in the XRD pattern in Fig. 1, consistent with incorporation of Ni atoms in the pyrite lattice. The sharp XRD peaks of these materials confirm these materials' crystallinity. The Ni-alloyed NCs have less adhesion to the sodalime glass, found during the fabrication of the thin films, compared to pure iron pyrite NCs. In agreement with a previous report,[39] the measured XRD diffraction pattern for $x = 0.5$ match excellently with the standard XRD pattern of bravoite ($Ni_{0.5}Fe_{0.5}S_2$) as obtained from MDI JADE. This fact is supported by the intermediate 2θ values of this material in the diffractogram presented in Fig. 1. For higher concentrations of Ni, $x = 0.75$ and $x = 1$, a peak was

observed at $2\theta \approx 50°$, which is tentatively assigned to be Ni_3S_4. Based on the XRD pattern analysis, these two sample compositions consist principally of pyrite NiS_2 with a small component of Ni_3S_4 NC material. The injection temperature and growth duration were not modified as a function of composition. The Ni_3S_4 exhibits face-centered cubic (FCC) crystal structure with a lattice constant (9.444 Å), larger than simple cubic (pyrite) NiS_2 NCs.[40] Phase pure NiS_2 NCs can be synthesized by adjusting the reaction temperature and/or growth time.[16,30,41] Pyrite (FeS_2) and vaesite (NiS_2) crystallize with the same cubic crystal structure (space group $Pa\bar{3}$) with lattice constants 5.430 Å and 5.686 Å respectively.[15,26] The standard XRD pattern data for NiS_2 was obtained from MDI JADE software (PDF# 98-001-3472), and is presented with vertical lines in Fig. 1. Based on the diffraction pattern, the lattice constants of these alloyed NCs can be obtained by using Bragg's law[42] and predicted lattice constant values can be predicted with Vegard's law.[43]

Similarly, the lattice constant (a) can be approximated based on the XRD pattern shown in Fig. 1. For the diffraction peak at Miller index (hkl), the lattice constant for cubic crystal structure is given by $a = d_{hkl}\sqrt{h^2 + k^2 + l^2}$ where d_{hkl} is the inter-plane lattice spacing obtained from Bragg's law, $2d_{hkl}\sin\theta = n\lambda$, where θ is Bragg's diffraction angle and λ is the wavelength of the X-ray used, and n is the order of diffraction ($n = 1$ in this case). Using this equation, the lattice constants for the diffraction peaks at Miller indices (111), (200), (210), (211), (220) and (311) were calculated, and the average lattice constant is presented in Table S1 (in ESI†). Additionally, Vegard's law can be employed to predict the lattice constants of alloyed composite material, and the lattice constants for different material composition is also included. The standard lattice constant values of iron pyrite (FeS_2) and vaesite (NiS_2) were taken to be 5.430 and 5.686 Å respectively for this calculation.[15,26] Previously, Ho *et al.* have reported the lattice constant of $Ni_{0.1}Fe_{0.9}S_2$ to be 5.435 Å for a single crystal grown by CVT method.[21] The XRD pattern for $Ni_{0.5}Fe_{0.5}S_2$ ($x = 0.5$) match with the standard diffraction pattern of the crystal bravoite ($Ni_{0.5}Fe_{0.5}S_2$) obtained from MDI JADE software (PDF #97-004-0329), and also the average lattice constant (5.569 Å) is very close to the lattice constant of crystal $Ni_{0.5}Fe_{0.5}S_2$, bravoite (5.570 Å).[39] All the lattice constant values obtained from diffraction pattern data and Vegard's law agree closely for up to $x = 0.5$ (Fig. 2). For higher concentration of Ni, the lattice constants based on the diffraction peaks are slightly higher than the calculated lattice constants using Vegard's law, perhaps owing to the formation of impurity compounds such as the FCC Ni_3S_4. The variation in experimental lattice constant with predicted (calculated) lattice constants is graphically shown in the Fig. 2. It is clear that Ni alloys well with iron in pyrite NCs, and the lattice constants change largely in accordance with the Vegard's law. Previously, Ferrer *et al.* studied the lattice constant variation with composition for $Fe_xNi_{1-x}S_2$ films prepared by flash-evaporation of Fe–Ni films with sulfuration at 350 °C, and our results reasonably agree with the previous report.[26]

The crystallite size, crystalline domain that can exist within the polycrystalline (or nanocrystalline) material, of these synthesized NCs have been estimated using the Debye–Scherrer equation,
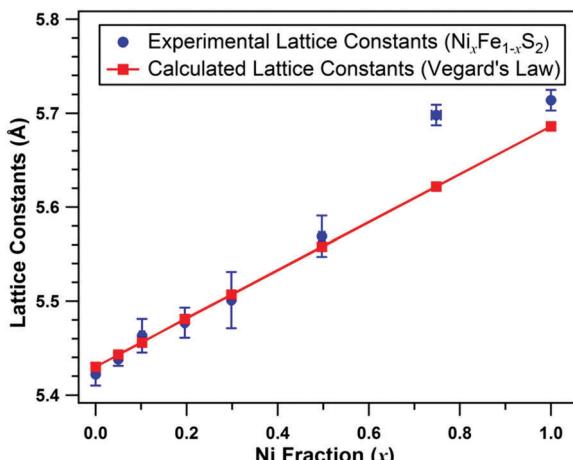
Fig. 2 Lattice constants for Ni-alloyed iron sulfide ($Ni_xFe_{1-x}S_2$) pyrite nanocrystals for seven different compositions. The experimental lattice constant values agree closely with the predicted lattice constant values (Vegard's law) up to the Ni fraction $x = 0.5$, and it is slightly too high for the highest concentrations of Ni.

$D_p = \dfrac{K\lambda}{\beta \cos\theta}$ where D_p is the crystallite size, K is the shape factor usually taken as close to unity, λ is the wavelength of the X-ray used, β (in radian) is the full width at half maximum (FWHM), and θ is the Bragg's diffraction angle.[44] Based on the XRD pattern presented in Fig. 1 above, Scherrer analysis has been carried to calculate the crystallite sizes of the Ni-alloyed iron pyrite NCs, and the results are summarized in Table 1. For this calculation, $K = 0.94$, wavelength (λ) = 0.154059 nm were taken, and the FWHM was calculated using OriginPro software for each diffraction peaks; $0.08°$ was subtracted from the FWHM values to account for X-ray source bandwidth broadening. The crystallite size estimation for $Ni_{0.75}Fe_{0.25}S_2$ and NiS_2 based on the diffraction peaks at Miller indices (210) and (220) were omitted due to less intense peaks compared to other peaks. Based on this analysis, the average crystallite sizes of the pure FeS_2 NCs is around 30 nm, slightly larger than the FeS_2 synthesized by injecting S precursor at 220 °C discussed in the previous report (though the particle sizes observed through the SEM imaging is similar).[33] For a Ni-fraction of $x = 0.05$, the average crystallite size is found to be 15 nm, and for other concentrations of Ni, Scherrer analysis yields similar crystallite

sizes in the range of 9 to 13 nm. Similarly, for pure NiS_2 the average crystallite size is $\sim$12 nm, substantially smaller than the size of pure FeS_2 NCs. In addition, scanning electron microscopy (SEM) images were acquired to investigate the surface morphology and particle size of the pure FeS_2 and Ni-alloyed FeS_2 NCs and thin films.

Fig. 3 displays the SEM images for typical iron pyrite (FeS_2) NCs and Ni-alloyed iron pyrite NCs. The shape of the pure FeS_2 NCs synthesized here are not as ideally cubic as reported previously for the case in which S precursor was injected at 220 °C.[33] In this work, we used a lower injection temperature of 170 °C, and the temperature was immediately increased to 220 °C for the growth of the NCs. The average particle size of these FeS_2 NCs in the SEM image is $\sim$80 nm which is higher than the size based on the Scherrer analysis (30 nm), indicating that the NCs consist typically of multiple crystallites. Similarly, the SEM images of other $Ni_xFe_{1-x}S_2$ compositions, $Ni_{0.1}Fe_{0.9}S_2$, $Ni_{0.2}Fe_{0.8}S_2$, and $Ni_{0.5}Fe_{0.5}S_2$, are shown in the Fig. 3(b–d); the micrographs indicate a gradual decrease in the size of the particles as Ni-fraction increases. Additionally, more non-uniformly shaped particles have been observed as the Ni is alloyed in the FeS_2 NCs. For $Ni_{0.1}Fe_{0.9}S_2$ NCs, the particle sizes are similar to
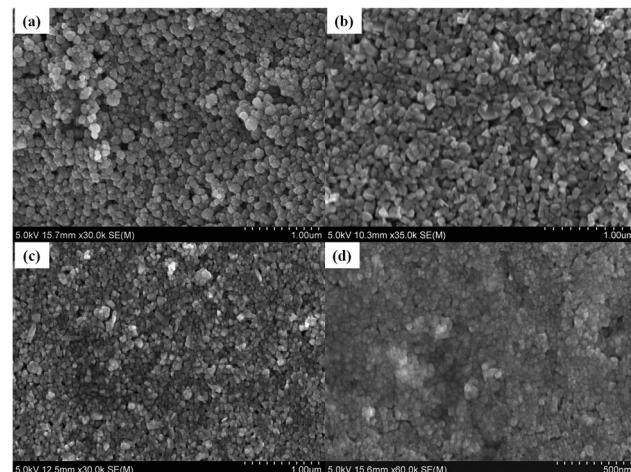

Fig. 3 Scanning electron microscopy (SEM) images of Ni-alloyed iron pyrite nanocrystals with different material compositions (a) FeS_2 NCs (b) $Ni_{0.1}Fe_{0.9}S_2$ NCs (c) $Ni_{0.2}Fe_{0.8}S_2$ NCs (d) $Ni_{0.5}Fe_{0.5}S_2$ NCs. The particle size of the alloyed NCs decreases as Ni fraction increases.

Table 1 Results of Scherrer analysis for the synthesized Ni-alloyed iron pyrite (FeS_2) nanocrystals based on the X-ray diffraction pattern shown in Fig. 1; majority carrier type is based on the sign of the thermal probe measurement

| S. No. | Material composition | Crystallite size based on the miller indices (nm) | | | | | Avg. crystallite size $\pm$ SD (D_p) (nm) | Majority carrier type |
		(200)	(210)	(211)	(220)	(311)		
1	FeS_2	32	33	34	29	21	30 ± 5	p
2	$Ni_{0.05}Fe_{0.95}S_2$	16	16	12	16	13	15 ± 2	p
3	$Ni_{0.1}Fe_{0.9}S_2$	13	10	9	14	11	11 ± 2	p
4	$Ni_{0.2}Fe_{0.8}S_2$	14	14	16	13	10	13 ± 2	n
5	$Ni_{0.3}Fe_{0.7}S_2$	12	20	6	5	6	10 ± 6	n
6	$Ni_{0.5}Fe_{0.5}S_2$	10	10	7	11	9	9 ± 2	n
7	$Ni_{0.75}Fe_{0.25}S_2$	16	—	8	—	13	12 ± 6	n
8	NiS_2	16	—	8	—	11	12 ± 4	n

the pure iron pyrite NCs but for the higher concentrations $Ni_{0.2}Fe_{0.8}S_2$ and $Ni_{0.5}Fe_{0.5}S_2$, the particle sizes are greatly reduced compared to pure FeS_2 NCs. The average particle size for $Ni_{0.5}Fe_{0.5}S_2$ NCs is around 20 nm as shown in the Fig. 3(d). However, the average crystallite size calculated using Scherrer-analysis based on the XRD pattern for $Ni_{0.5}Fe_{0.5}S_2$ NCs is around 9 nm which is even smaller.

The Raman spectra of three different NCs are presented in Fig. S2 (in ESI†) for pure FeS_2, $Ni_{0.5}Fe_{0.5}S_2$ and NiS_2 NCs. For pure FeS_2, the Raman active peaks were found to be at 341, 375 and 425 cm^{-1} as shown in Fig. S2(a) (ESI†). These peaks match closely with the previous reports, and based on the literature these Raman active peaks correspond to E_g, A_g, and T_g modes of vibration respectively.[18,21,33,45] Similarly, for $Ni_{0.5}Fe_{0.5}S_2$ the Raman active peaks were found to be at 325 and 388 cm^{-1} as presented in Fig. S2(b) (ESI†). Khalid et al. reported similar Raman active peaks at 339, 375 and 410 cm^{-1} for $Ni_xFe_{1-x}S_2$ thin films with $x = 0.1$, and these peaks correspond to E_g, A_g, and T_g modes of vibration respectively.[23] The Raman active peaks in NiS_2 were found to be at 287 and 477 cm^{-1} as shown in Fig. S2(c) (ESI†). Using a 488 nm laser for a NiS_2 single crystal, Suzuki et al. observed the Raman active peaks corresponding to the E_g and A_g modes at 281 cm^{-1} and 480 cm^{-1} respectively.[45] Similarly, Yang et al. have previously reported the Raman active modes of NiS_2 at 270 cm^{-1} and 476 cm^{-1} which agree reasonably with these observed peaks for NiS_2 NCs.[31] Further, Faber et al. have reported Raman peaks at 282 and 477 cm^{-1} similar to our results excited with 532 nm laser.[18] These Raman active peaks present in these nanocrystalline materials confirm the synthesized materials are high-purity FeS_2, Ni-alloyed FeS_2, and NiS_2 NCs. Further, the absorbance spectra in the range of 400 to 2000 nm are shown in Fig. 4 for pure FeS_2, $Ni_{0.5}Fe_{0.5}S_2$ and NiS_2 NCs. For pure FeS_2 NCs, the absorbance is close to zero in the far infrared (IR) region. The absorbance spectrum of FeS_2 NCs is similar to the previous results, and the absorbance rises strongly in a wavelength ≤ 1200 nm.
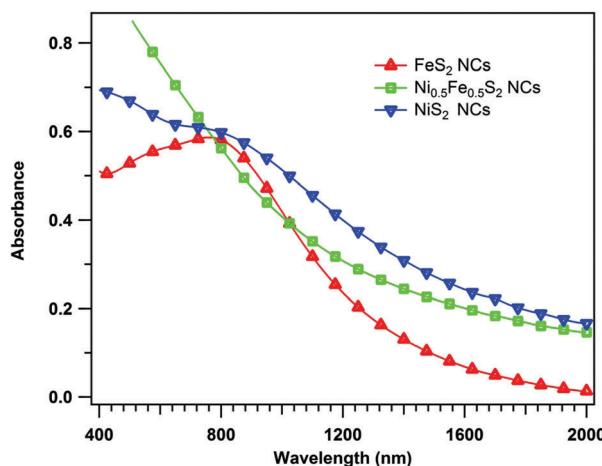

Fig. 4 UV-Vis-NIR absorption spectra of Ni-alloyed ($Ni_xFe_{1-x}S_2$) iron pyrite NCs with different material composition pure FeS_2 NCs, $Ni_{0.5}Fe_{0.5}S_2$ NCs and NiS_2 NCs solution dispersed in chloroform. Symbol point spacing is greater than the actual data point spacing.

It supports the strong absorption coefficient value of these NCs in the visible region similar to the previous reports.[14,33] For $Ni_{0.5}Fe_{0.5}S_2$ NCs, the absorbance value increases sharply at a wavelength of around 1000 nm, and the absorbance is relatively higher in the range 1200–2000 nm than FeS_2 NCs. In Ni-alloyed FeS_2, the observed non-zero absorption in the range 1200–2000 nm are the mid-gap absorption due to electrons photo-activated into the conduction band.[24] As shown in Fig. 4, the optical absorption spectrum for NiS_2 NCs shows features in the visible region which differ from the spectra of the alloyed $Ni_xFe_{1-x}S_2$ NC materials. The absorption feature in the IR region may be due to presence of other secondary phase material such as Ni_3S_4 as already discussed above. In addition, the IR absorption feature indicates a higher density of mid-gap states, and the metallic characteristics of these materials.

To understand the majority charge carrier type in alloyed composite NCs, a thermal probe measurement using a lab constructed apparatus was employed for thin films fabricated with different Ni concentration; results have been summarized in Table 1. The thermal probe technique allows rapid measurement of the sign of the thermoelectric effect via measurement of the voltage induced between the two probes, when one is heated.[14,46] As shown in Table 1, thermal probe measurement shows that for Ni-fraction with $x \geq 0.20$ in $Ni_xFe_{1-x}S_2$ show n-type behavior. Previously, Lehner et al. have also reported the change in conductivity of the iron pyrite films from p-type to n-type by doping with Ni atoms.[24,47] Similarly, the authors found these NiS_2 films to be n-type based on thermal probe measurement and Mott–Schottky analysis.[28] Further, Ho et al. have reported Ni as n-type dopant in FeS_2 single crystals, and it behaves like a donor level existed near the conduction band edge of the synthetic FeS_2 crystals.[21] It means that for iron pyrite NCs, the majority charge carriers are holes and for n-type alloyed materials, the majority charge carriers are electrons. Thus, based on this thermal probe measurement, it is interesting to note that on adding 20% or higher Ni concentration, iron sulfide NCs changes from p-type to n-type material.

In addition to this, Hall-effect measurements were carried out to investigate the mobility, carrier density, and Hall-coefficients of these alloyed composite materials. Table 2 shows the results of Hall-effect measurements carried out on drop-casted thin films on pre-cleaned sodalime glass of 1.5 cm × 1.5 cm; the average thickness for each film was ∼1 μm using van der Pauw geometry. For pure FeS_2 NCs, the carrier concentration (carrier density), and mobility were $\sim 10^{18}$ cm^{-3} and ~ 0.16 cm^2 V^{-1} s^{-1} similar to our previous results.[14,33] The charge carriers' type matched to the result determined by thermal probe measurement. P-type conductivity with holes as majority charge carriers for undoped iron pyrite prepared by evaporation have been reported elsewhere.[26,48] The Hall-effect measurement values for $x = 0.05$ and 0.1 in $Ni_xFe_{1-x}S_2$ alloys were similar to pure FeS_2 NCs. However, in case of $Ni_{0.2}Fe_{0.8}S_2$ NCs, the resistivity observed was higher than FeS_2 NCs, and the majority charge carriers were electrons similar to thermal probe measurement. For 50% Ni-doped iron pyrite, the carrier density was found to be in the order of 10^{15} cm^{-3} with a very high mobility of ~ 101 cm^2 V^{-1} s^{-1}. In our case, the mobility in alloyed NCs is found to be greatly

Table 2 Hall-effect measurement of Ni-alloyed iron sulfide ($Ni_xFe_{1-x}S_2$) pyrite nanocrystals (NCs)

Hall parameters	Material composition					
	FeS_2 NCs	$Ni_{0.05}Fe_{0.95}S_2$ NCs	$Ni_{0.1}Fe_{0.9}S_2$ NCs	$Ni_{0.2}Fe_{0.8}S_2$ NCs	$Ni_{0.5}Fe_{0.5}S_2$ NCs	NiS_2 NCs
Resistivity (Ω cm)	6.27 ± 0.03	6.25 ± 0.04	6.35 ± 0.02	11.45 ± 1.02	58.48 ± 0.03	1.46 ± 1.10
Mobility ($cm^2\ V^{-1}\ s^{-1}$)	0.16 ± 0.08	0.30 ± 0.10	0.17 ± 0.03	-0.91 ± 0.05	$-(101.49 \pm 3.02)$	$-(0.09 \pm 0.06)$
Charge density (cm^{-3})	$7.2(\pm 2.5) \times 10^{18}$	$3.84(\pm 0.7) \times 10^{19}$	$1.53(\pm 0.72) \times 10^{19}$	$6.56(\pm 3.02) \times 10^{18}$	$(1.1 \pm 0.4) \times 10^{15}$	$(6.5 \pm 1.7) \times 10^{19}$
Hall coeff. ($cm^3\ Coul^{-1}$)	1.08 ± 0.49	0.17 ± 0.03	0.47 ± 0.17	$-(0.58 \pm 0.33)$	$-(5.93 \pm 0.17) \times 10^3$	$-(0.11 \pm 0.03)$
Sheet resistance ($\Omega\ \square^{-1}$)	$6.3(\pm 0.2) \times 10^4$	$6.2(\pm 0.4) \times 10^4$	$6.2(\pm 0.2) \times 10^4$	$7.2(\pm 0.2) \times 10^6$	$1.2(\pm 0.6) \times 10^6$	$2.7(\pm 0.4) \times 10^4$
Carriers	Holes	Holes	Holes	Electrons	Electrons	Electrons

enhanced compared to undoped iron pyrite NCs, and the results agree with the previous reports. For example, Lehner *et al.* have reported the carrier concentration $\sim 4 \times 10^{16}$ cm^{-3} for Ni-doped iron pyrite single crystals, and with higher mobility 130 cm^2 V^{-1} S^{-1}.[47] The sheet resistance for x = 0.05, 0.1 in alloyed NCs are similar to pure FeS_2 NCs ($\sim 10^4$ Ω $\square^{-1}$), but higher for x = 0.2 and 0.5 ($\sim 10^6$ Ω $\square^{-1}$). However, Ho *et al.* have reported the resistivity values for Ni-alloyed iron pyrite single crystals to be decreased with higher Ni concentration.[21] Similarly, the charge carrier density in pure NiS_2 thin films was found to be $\sim 10^{19}$ cm^{-3}, higher than the value reported by Chate *et al.* ($\sim 10^{17}$ cm^{-3}).[49] For NiS_2 NCs, the charge carriers' type was found to be electrons similar to the results reported previously.[28,47] Higher carrier concentration observed in the NiS_2 NCs may be due to the smaller particle size creating large number of defects at the boundaries, and these defects may be attributed to unpassivated surface dangling bonds.[50]

Our laboratory uses copper/gold (Cu/Au) as the standard back contact material for CdTe solar cells,[51,52] though we are actively working to establish an improved back contact which enables inexpensive processing, and a low potential barrier for hole transport so as to achieve finished photovoltaic devices with excellent performance and stability. In the case of Cu/Au, we typically observe a potential barrier for the transport of holes at the back contact since the valence band edge of CdTe is deeply located ~ 5.8 eV below the vacuum level,[53] and the work function of Au is ~ 5.0 eV.[54] The Cu treatment serves to increase the free hole concentration at the contact to Au, thereby narrowing the barrier width to allow efficient thermionic emission across the barrier. Iron pyrite (FeS_2) NCs, with high hole density ($p \sim 10^{19}$ cm^{-3}) has been shown to reduce the effective barrier when used as an HTL on CdTe, improving performance.[35,55] Here, we are interested to investigate the effect of material composition by using Ni-alloyed iron pyrite NC ($Ni_xFe_{1-x}S_2$) film as a HTL to CdTe devices. A schematic device structure and the cross-sectional SEM image are presented in Fig. 5. The Ni concentration was varied from x = 0 to x = 0.3 and 5 different compositions were tested as interface layers. During the deposition of the NCs, a thickness of ~ 1.5 μm was preferred to avoid the pinholes and the good coverage of the CdTe absorbing layer. After the device fabrication, the *J–V* characteristics and external quantum efficiency (EQE) of the devices were measured.

Fig. 6 displays the *J–V* characteristics and external quantum efficiencies of CdS/CdTe solar cells with Ni-alloyed iron pyrite NCs as back contacts. In case of Cu/Au back contacts, the best
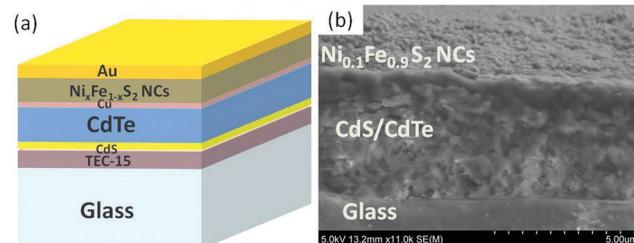
Fig. 5 Device structure of CdTe solar cell using $Ni_xFe_{1-x}S_2$ as back contact material (a) schematic diagram of the device structure (b) cross-sectional SEM image of CdS/CdTe solar cells with $Ni_{0.1}Fe_{0.9}S_2$ NCs as interface layer.

device has an efficiency (η) of 11.6% with open-circuit voltage (V_{OC}) 826 mV, short-circuit current-density (J_{SC}) 19.12 mA cm^{-2}, and fill factor (FF) of 74%. The average parameters of twenty cells for Cu/Au back contacts are displayed in Table 3. Similarly, when iron pyrite NCs film was used as an HTL, the best device efficiency was found to be 11.9% with a V_{OC} of 831 mV, J_{SC} of 20.1 mA cm^{-2}, and FF = 71%. For Cu/FeS_2-NC/Au back contacted devices, the average efficiency is increased by ~ 4% than Cu/Au back contacts (Table 3). These results reasonably agree well with our previous reports.[35,55] We attribute the slight enhancement in device performance to the increase in V_{OC} and J_{SC} though the FF was decreased. The increase in J_{SC} was verified by measuring the external quantum efficiency (EQE), in which the quantum efficiency having FeS_2 layer as an interface layer is slightly higher than Cu/Au back contacts in the range of 550 to 800 nm as shown in Fig. 6(b). The observed increase in performance is contributed due to the effective transport of the charge carriers towards the back contacts of the device.[35,36] Our interest in this paper is to see the effect of $Ni_xFe_{1-x}S_2$ in the performance of CdTe solar cells. When $Ni_{0.05}Fe_{0.95}S_2$ NCs film is used, the average efficiency increased by ~ 5% and reached 12.1%, whereas for $Ni_{0.1}Fe_{0.9}S_2$ NCs, the device performance was similar to the iron pyrite NCs. The device efficiency with $Ni_{0.2}Fe_{0.8}S_2$ NCs as the interface material was found to be ~ 5% with the decrease of 56% than the standard Cu/Au back contacts, and with $Ni_{0.3}Fe_{0.7}S_2$ NCs, the device efficiency was ~ 2%. The decrease in device performance was attributed to the decrease in the J_{SC} and FF, and the typical *J–V* characteristics are shown in Fig. 6(a). To verify the current-densities obtained from *J–V* measurements, the EQEs were measured and integrated, as presented in Fig. 6(b). Based on these EQE measurements, the current densities for $Ni_{0.2}Fe_{0.8}S_2$ and $Ni_{0.3}Fe_{0.7}S_2$ NCs interface layers were found
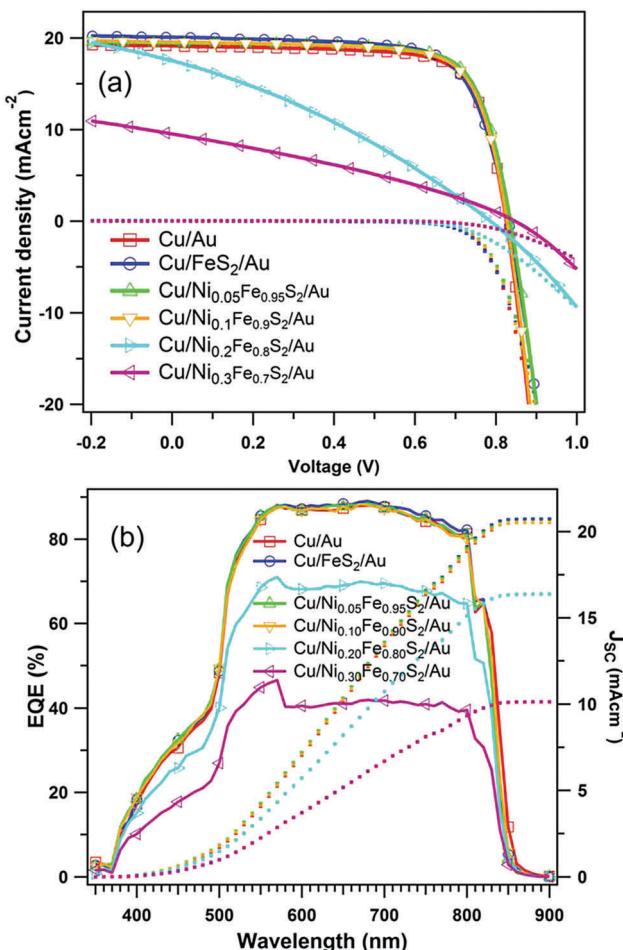
Fig. 6 Device performance when $Ni_xFe_{1-x}S_2$ NCs films were used as interface layers in CdTe solar cells: (a) $J–V$ characteristics with AM 1.5G simulated irradiance, and (b) external quantum efficiencies (EQEs).

the n-type conductivity for 20% (or higher) Ni-alloyed iron pyrite NCs, indicating electrons as the majority charge carriers (Table 1). The increase in V_{OC} for 20% and 30% Ni-alloyed NCs is different from our expectance for materials having n-type conductivity. The increase in series resistance indicates that materials are resistive than 5% or 10% Ni-alloyed NCs, and hence makes more difficult for the charge transport. A point to be noted here is there was no heat treatment applied during the fabrication of the interface layer due to which the intermixing of CdTe with the NCs at the interface layer is minimum because the room temperature thermal energy is not sufficient to diffuse the ions into the opposite side. Further, we are currently working to understand the behavior of these n-type NC materials at the back contact in CdTe devices.

Conclusion

Here, we have successfully synthesized and characterized Ni-doped iron pyrite NCs and found that the electronic conductivity depends upon the composition of the material. When the concentration of Ni in the iron pyrite NCs becomes 20% or higher, the majority charge carrier type changes from p-type (holes) to n-type (electrons). These Ni-alloyed iron sulfide ($Ni_xFe_{1-x}S_2$) NCs exhibit cubic crystal structure in pyrite phase. Further, as the Ni concentration increases in the iron pyrite (FeS_2) NCs, the XRD diffraction peaks shift towards lower 2θ values which clearly indicate the increase in the lattice constant due to the incorporation of Ni in the crystal lattices. The experimentally determined lattice constants match well with the predicted lattice constants (Vegard's law) up to the Ni concentration of 50%. Based on Scherrer analysis, the particle sizes decrease as the Ni concentration increases, in agreement with the results of SEM imaging. The absorbance values in the Ni-alloyed NCs in IR region is higher as the Ni fraction increases, ascribed to the increased metallic behavior and/or increased mid-band defect states in Ni-doped iron pyrite NCs. The thermal injection synthesis method demonstrated here can be generalized for the synthesis of other similar colloidal nanocrystalline materials. Additionally, these $Ni_xFe_{1-x}S_2$ NCs for $x = 0$ to 0.1 can be applied as the HTL to improve the device performance in the CdS/CdTe solar cells. Based on our study, $Ni_{0.05}Fe_{0.95}S_2$ NC-based HTL improved the CdS/CdTe device efficiency by $\sim5\%$ as compared with our laboratory standard back contact. Nanocrystalline materials such as FeS_2 and NiO have been applied as the HTL for efficient perovskite solar cells, and these $Ni_xFe_{1-x}S_2$ NCs may find a similar role in energy harvesting applications.

to be 16.3 mA cm^{-2} and 10.1 mA cm^{-2}, respectively which agree well with the values obtained from $J–V$ measurement. This decrease in the device efficiency is also attributed to the strong decrease in the FF of the solar cells. The significant increase in the series resistance and the strong decrease in the shunt resistance of the devices for both 20% and 30% Ni-alloyed NCs are the main cause of poor performance. Based on these measurements, the properties of 20% and 30% Ni-alloyed NCs are different from 5% and 10% Ni-alloyed NCs, which may be due to the change in conductivity and/or the change in majority carrier type in the HTL. The thermal probe measurement shows

Table 3 Summary of the $J–V$ characteristics of the twenty CdS/CdTe solar cells when using $Ni_xFe_{1-x}S_2$ as the interface layers. The $\pm$ value represents the standard deviation (SD) of the measured device parameters

Back contacts	V_{OC} (mV)	J_{SC} (mA cm^{-2})	Fill factor (FF%)	Efficiency (η%)
Cu/Au	829 $\pm$ 2	18.9 $\pm$ 0.2	71.1 $\pm$ 2.3	11.2 $\pm$ 0.4
Cu/FeS$_2$ NCs/Au	834 $\pm$ 2	20.2 $\pm$ 0.2	68.8 $\pm$ 0.8	11.6 $\pm$ 0.4
Cu/Ni$_{0.05}$Fe$_{0.95}$S$_2$ NCs/Au	835 $\pm$ 3	19.7 $\pm$ 0.3	70.8 $\pm$ 1.8	11.8 $\pm$ 0.3
Cu/Ni$_{0.1}$Fe$_{0.9}$S$_2$ NCs/Au	835 $\pm$ 2	19.1 $\pm$ 0.1	70.5 $\pm$ 0.9	11.5 $\pm$ 0.3
Cu/Ni$_{0.2}$Fe$_{0.8}$S$_2$ NCs/Au	842 $\pm$ 1	17.7 $\pm$ 2.5	32.3 $\pm$ 2.6	4.8 $\pm$ 1.0
Cu/Ni$_{0.3}$Fe$_{0.7}$S$_2$ NCs/Au	848 $\pm$ 1	8.7 $\pm$ 3.9	30.6 $\pm$ 2.4	2.2 $\pm$ 1.1

Acknowledgements

References

1 M. Cabán-Acevedo, D. Liang, K. S. Chew, J. P. DeGrave, N. S. Kaiser and S. Jin, *ACS Nano*, 2013, **7**, 1731–1739.

2 M. Limpinsel, N. Farhi, N. Berry, J. Lindemuth, C. L. Perkins, Q. Lin and M. Law, *Energy Environ. Sci.*, 2014, **7**, 1974–1989.

3 C. Wadia, A. P. Alivisatos and D. M. Kammen, *Energy Environ. Sci.*, 2009, **43**, 2072–2077.

4 A. Ennaoui, S. Fiechter, C. Pettenkofer, N. Alonso-Vante, K. Büker, M. Bronold, C. Höpfner and H. Tributsch, *Sol. Energy Mater. Sol. Cells*, 1993, **29**, 289–370.

5 F. Liu, J. Zhu, L. Hu, B. Zhang, J. Yao, M. K. Nazeeruddin, M. Gratzel and S. Dai, *J. Mater. Chem. A*, 2015, **3**, 6315–6323.

6 M.-R. Gao, Y.-F. Xu, J. Jiang and S.-H. Yu, *Chem. Soc. Rev.*, 2013, **42**, 2986–3017.

7 D. Liang, R. Ma, S. Jiao, G. Pang and S. Feng, *Nanoscale*, 2012, **4**, 6265–6268.

8 V. K. Gudelli, V. Kanchana, G. Vaitheeswaran, M. C. Valsakumar and S. D. Mahanti, *RSC Adv.*, 2014, **4**, 9424–9431.

9 J. Hu, Y. Zhang, M. Law and R. Wu, *J. Am. Chem. Soc.*, 2012, **134**, 13216–13219.

10 B. Mao, Q. Dong, Z. Xiao, C. L. Exstrom, S. A. Darveau, T. E. Webber, B. D. Lund, H. Huang, Z. Kang and J. Huang, *J. Mater. Chem. A*, 2013, **1**, 12060–12065.

11 R. Sun and G. Ceder, *Phys. Rev. B: Condens. Matter Mater. Phys.*, 2011, **84**, 245211.

12 P. Xiao, X.-L. Fan, H. Zhang, X. Fang and L.-M. Liu, *J. Alloys Compd.*, 2015, **629**, 43–48.

13 K. Büker, S. Fiechter, V. Eyert and H. Tributsch, *J. Electrochem. Soc.*, 1999, **146**, 261–265.

14 T. Kinner, K. P. Bhandari, E. Bastola, B. M. Monahan, N. O. Haugen, P. J. Roland, T. P. Bigioni and R. J. Ellingson, *J. Phys. Chem. C*, 2016, **120**, 5706–5713.

15 J. Wilson, *Adv. Phys.*, 1972, **21**, 143–198.

16 H. Pang, C. Wei, X. Li, G. Li, Y. Ma, S. Li, J. Chen and J. Zhang, *Sci. Rep.*, 2014, **4**, 3577.

17 C.-H. Lai, M.-Y. Lu and L.-J. Chen, *J. Mater. Chem.*, 2012, **22**, 19–30.

18 M. S. Faber, M. A. Lukowski, Q. Ding, N. S. Kaiser and S. Jin, *J. Phys. Chem. C*, 2014, **118**, 21347–21356.

19 M. Gong, D.-Y. Wang, C.-C. Chen, B.-J. Hwang and H. Dai, *Nano Res.*, 2016, **9**, 28–46.

20 M. Bronold, S. Kubala, C. Pettenkofer and W. Jaegermann, *Thin Solid Films*, 1997, **304**, 178–182.

21 C. H. Ho, C. E. Huang and C. C. Wu, *J. Cryst. Growth*, 2004, **270**, 535–541.

22 S. Khalid, E. Ahmed, M. Azad Malik, D. J. Lewis, S. Abu Bakar, Y. Khan and P. O'Brien, *New J. Chem.*, 2015, **39**, 1013–1021.

23 S. Khalid, M. A. Malik, D. J. Lewis, P. Kevin, E. Ahmed, Y. Khan and P. O'Brien, *J. Mater. Chem. C*, 2015, **3**, 12068–12076.

24 S. W. Lehner, K. S. Savage and J. C. Ayers, *J. Cryst. Growth*, 2006, **286**, 306–317.

25 K. Anuar, W. Tan, M. Jelas, S. Ho, S. Gwee and N. Saravanan, *Thammasat Int. J. Sci. Technol.*, 2010, **15**, 62–69.

26 I. J. Ferrer, C. D. L. Heras and C. Sanchez, *J. Phys.: Condens. Matter*, 1995, **7**, 2115.

27 I. J. Ferrer and C. Sánchez, *J. Appl. Phys.*, 1991, **70**, 2641–2647.

28 K. Rajes, M. Zaidan and A. Aziz, *Rep. Electrochem.*, 2013, **3**, 25–29.

29 J. Hu, Q. Lu, B. Deng, K. Tang, Y. Qian, Y. Li, G. Zhou and X. Liu, *Inorg. Chem. Commun.*, 1999, **2**, 569–571.

30 Q. Xuefeng, L. Yadong, X. Yi and Q. Yitai, *Mater. Chem. Phys.*, 2000, **66**, 97–99.

31 S.-L. Yang, H.-B. Yao, M.-R. Gao and S.-H. Yu, *CrystEngComm*, 2009, **11**, 1383–1390.

32 J. Puthussery, S. Seefeld, N. Berry, M. Gibbs and M. Law, *J. Am. Chem. Soc.*, 2011, **133**, 716–719.

33 K. P. Bhandari, P. J. Roland, T. Kinner, Y. Cao, H. Choi, S. Jeong and R. J. Ellingson, *J. Mater. Chem. A*, 2015, **3**, 6853–6861.

34 E. Bastola, K. P. Bhandari, A. J. Matthews, N. Shrestha and R. J. Ellingson, *RSC Adv.*, 2016, **6**, 69708–69714.

35 K. P. Bhandari, P. Koirala, N. R. Paudel, R. R. Khanal, A. B. Phillips, Y. Yan, R. W. Collins, M. J. Heben and R. J. Ellingson, *Sol. Energy Mater. Sol. Cells*, 2015, **140**, 108–114.

36 A. J. Huckaba, P. Sanghyun, G. Grancini, E. Bastola, C. K. Taek, L. Younghui, K. P. Bhandari, C. Ballif, R. J. Ellingson and M. K. Nazeeruddin, *ChemistrySelect*, 2016, **1**, 5316–5319.

37 L. Calió, S. Kazim, M. Grätzel and S. Ahmad, *Angew. Chem., Int. Ed.*, 2016, **55**, 14522–14545.

38 W. Wang, X. Pan, W. Liu, B. Zhang, H. Chen, X. Fang, J. Yao and S. Dai, *Chem. Commun.*, 2014, **50**, 2618–2620.

39 D. C. H. W. Petruck and J. M. Stewart, *Can. Mineral.*, 1969, **9**, 597–616.

40 Q. Liu, A. Diaz, A. Prosvirin, Z. Luo and J. D. Batteas, *Nanoscale*, 2014, **6**, 8935–8942.

41 L. Zhang, J. C. Yu, M. Mo, L. Wu, Q. Li and K. W. Kwong, *J. Am. Chem. Soc.*, 2004, **126**, 8116–8117.

42 W. H. Bragg and W. L. Bragg, *Proc. R. Soc. London, Ser. A*, 1913, **88**, 428–438.

43 L. Vegard, *Z. Phys.*, 1921, **5**, 17–26.

44 J. I. Langford and A. Wilson, *J. Appl. Crystallogr.*, 1978, **11**, 102–113.

45 T. Suzuki, K. Uchinokura, T. Sekine and E. Matsuura, *Solid State Commun.*, 1977, **23**, 847–852.

46 A. Axelevitch and G. Golan, *Facta universitatis-series: Electronics and Energetics*, 2013, **26**, 187–195.

47 S. W. Lehner, N. Newman, M. van Schilfgaarde, S. Bandyopadhyay, K. Savage and P. R. Buseck, *J. Appl. Phys.*, 2012, **111**, 083717.

48 I. J. Ferrer, J. R. Ares and C. R. Sánchez, *Sol. Energy Mater. Sol. Cells*, 2003, **76**, 183–188.

49 P. A. Chate and D. J. Sathe, *Appl. Phys. A: Mater. Sci. Process.*, 2016, **122**, 1–5.

50 C. Clark and S. Friedemann, *J. Magn. Magn. Mater.*, 2016, **400**, 56–61.

51 E. Janik and R. Triboulet, *J. Phys. D: Appl. Phys.*, 1983, **16**, 2333.

52 C. R. Corwine, A. O. Pudov, M. Gloeckler, S. H. Demtsu and J. R. Sites, *Sol. Energy Mater. Sol. Cells*, 2004, **82**, 481–489.

53 J. L. Freeouf and J. M. Woodall, *Appl. Phys. Lett.*, 1981, **39**, 727–729.

54 B. de Boer, A. Hadipour, M. M. Mandoc, T. van Woudenbergh and P. W. M. Blom, *Adv. Mater.*, 2005, **17**, 621–625.

55 K. P. Bhandari, X. Tan, P. Zereshki, F. K. Alfadhili, A. B. Phillips, P. Koirala, M. J. Heben, R. W. Collins and R. J. Ellingson, *Sol. Energy Mater. Sol. Cells*, 2017, **163**, 277–284.